CEAS Space Journal
https://doi.org/10.1007/s12567-024-00580-w

ORIGINAL PAPER

Multi-physics simulation study of magnetic shielding on hypersonic vehicles

Thomas J. Greenslade[1] · Arun Kumar Chinnappan[1] · Minkwan Kim[1]

Received: 8 July 2024 / Revised: 14 November 2024 / Accepted: 18 November 2024

Abstract
The renewed interest in hypersonic flights due to NASA's Artemis program has brought fresh attention to the physical challenges of reusable thermal protection systems. The need to enhance the reliability of hypersonic and re-entry vehicles has sharply focused on the limitations of our current comprehension of thermo-chemical non-equilibrium flows and our limited predictive capabilities. This paper presents the work carried out by the University of Southampton and our consortium partners within the MEESST collaboration. This project is currently involved in both numerical and experimental research to develop magnetic shielding techniques for atmospheric re-entry vehicles. These techniques aim to offer additional approaches for mitigating both impinging heat loads and communication blackout. Herein, we present the results of multi-physics simulations conducted with the University of Southampton's HANSA toolkit, along with comparisons, both experimental and numerical, produced by our consortium partners. These encompass simulations of multiple capsules undergoing atmospheric re-entry and simulations of ground-based experimental campaigns. We give particular attention to the effects of thermo-chemical non-equilibrium and MHD modelling. We illustrate the impacts of various mathematical models on the results obtained, with a strong emphasis on mission-critical parameters such as surface heat fluxes and electron densities. We also present conclusions regarding the implications of these results on magnetic shielding designs. Lastly, we offer an overview of current knowledge gaps in areas crucial to MEESST and lay out plans for future simulations and experiments, both within the MEESST project and beyond.

Keywords MEESST · MHD · TPS · HANSA · Heatshield · Re-entry · Hypersonic

Abbreviations

B	Magnetic field
E	Total energy
E_{ve}	Vibrational-electronic energy
E_e	Electron energy
q_{tr}	Translational-rotational heat flux
q_{ve}	Vibrational-electronic heat flux
q_e	Electron heat flux
τ	Viscous stress tensor
u, v, w	Flow velocities in x, y and z directions
ρ_i	Density of species
p	Pressure
δ_{ij}	Kronecker delta
Y	Molar fraction
S	Source term in the Navier–Stokes equation

✉ Arun Kumar Chinnappan
a.chinnappan@soton.ac.uk

Thomas J. Greenslade
t.greenslade@soton.ac.uk

Minkwan Kim
m.k.kim@soton.ac.uk

[1] University of Southampton, University Road, Southampton SO17 1BJ, UK

1 Introduction

Returning to Earth after spaceflight presents significant challenges, and there has been a notable resurgence of interest in both interplanetary and terrestrial spaceflight over the past decade. During atmospheric re-entry, the kinetic energy of a gas is converted into heat after the shock, raising the vehicle's surface temperature to extreme values (~ 20,000 K). This high thermal load (~ 300 kJ/cm^2 on Galileo [1], 6 kJ/cm^2 on the Mars Science Laboratory [2]) experienced during atmospheric re-entry necessitates the use of a thermal protection system (TPS) to absorb and dissipate the substantial heating in order to safeguard the vehicle from the extreme heat environment. Some alternative techniques have been

Published online: 03 December 2024

proposed to reduce heat transfer during re-entry, such as spiking forebodies [3, 4], transpiration cooling [5–7], and gas jet injection [8, 9], however, these methods face practical limitations. Hence, TPS is still being used in the re-entry vehicles considering the safety margin. While both ablating and non-ablating TPS are available, ablating TPS is more commonly used because of its ability to withstand higher heat loads through the process of phase change and mass loss. Ablative TPS materials typically consist of carbon or silica fibres embedded within a phenolic resin matrix. In this process, heat is absorbed by the phenolic resin and is removed as the material ablates away. As a result, ablative TPS is heavy, often constituting up to 30% of a re-entry vehicle's mass and is not reusable, thus significantly increasing the mission cost.

Moreover, the very high temperatures after the bow shock induce various chemical reactions within the surrounding gas, including dissociation–recombination, exchange reactions, and ionisation in the near-surface region. This intense ionisation generates a thin, dense layer of electrons known as the plasma sheath, enveloping the vehicle. This plasma sheath could effectively block the propagation of electromagnetic waves when the plasma frequency exceeds the radio wave frequency, resulting in what is commonly known as a radio or communication blackout [10, 11]. Although the radio blackout was initially observed during the early space race, it remains a challenge for capsule-shaped vehicles, both manned and unmanned missions. Several techniques, including aerodynamic shaping, quenchant injection, higher communication frequencies, and Raman scattering, have been proposed to mitigate radio blackouts during re-entry [11, 12]. However, these methods are case-specific and have practical limitations.

As a novel solution for these above-mentioned challenges encountering during atmospheric re-entry, the Magneto-hydrodynamic (MHD) Enhanced Entry System for Space Transportation (MEESST) project aims to manipulate plasma layer and heat flux of a vehicle using MHD effects. The MEESST project consists of a consortium of partner institutions, academic and industrial, each contributing specialist expertise in both numerical and experimental plasma dynamics. The consortium consists of academic institutions at; the Karlsruhe Institute of Technology (KIT), the University of Stuttgart's Institute of Space Systems (IRS), the University of Southampton, the Catholic University of Leuven (KU Leuven), the Von Karman Institute for Fluid Dynamics (VKI) and the University of Luxembourg. In addition, the consortium includes industrial institutions; Advanced Engineering Design Solutions (AEDS), THEVA, Neutron Star Systems and Absolut System.

MEESST's approach primarily relies on harnessing the Lorentz force to control the behaviour of the plasma enveloping the spacecraft, effectively minimizing thermal interaction between the harsh entry environment and the vehicle's surface materials [13]. Furthermore, the MEESST magnetic system exhibits the potential to offer supplementary advantages to space vehicles, including radiation shielding [14, 15]. This study focuses on the numerical investigations conducted by the University of Southampton and provides comparisons with experimental and numerical data generated by our consortium partners.

Given the complexities of this problem, which involve several non-equilibrium processes, we have employed an in-house Computational Fluid Dynamics (CFD) solver incorporating thermo-chemical non-equilibrium models coupled with MHD models. This study specifically explores the influence of thermo-chemical non-equilibrium and MHD models on predicting radio blackout and heat flux manipulation during re-entry. The remainder of this paper is arranged as follows: Sect. 2 details the numerical modelling, Sect. 3 presents solver validation along with results and discussion, and Sect. 4 concludes the paper and outlines the future work.

2 Numerical modelling

2.1 Governing equations

The governing equations for the MEESST system are principally composed of two parts, which are the flow field and the MHD field. These equations describe a thermo-chemical non-equilibrium flow with MHD effects, Lorentz force and Joule heating. The governing equations of the flow field with the MHD effect, therefore, can be expressed in the following form:

$$\frac{\partial \mathbf{Q}}{\partial t} + \nabla \cdot \left(\mathbf{F} - \mathbf{F}_v\right) = \mathbf{S}_{NEQ} + \mathbf{S}_{MHD} \tag{1}$$

where $\mathbf{Q}$ is the vector of conservative variables, $\mathbf{F}$ is the inviscid flux vector, and $\mathbf{F}_v$ is the viscous flux vector, $\mathbf{S}_{NEQ}$ is the thermochemical non-equilibrium source terms and $\mathbf{S}_{MHD}$ is the source term related to MHD effects. The vector of conserved variables, $\mathbf{Q}$, is given by

$$\mathbf{Q} = \begin{Bmatrix} \rho_1 \\ \rho_2 \\ \vdots \\ \rho_s \\ \rho u \\ \rho v \\ \rho w \\ E \\ E_{ve} \\ E_e \end{Bmatrix} \tag{2}$$

where ρ_i is the density of species i, u, v and w are flow velocities, E is the total energy, E_{ve} is the vibrational-electronic energy, and E_e is the electron energy. The inviscid flux vector, $\mathbf{F}$, and viscous flux vector, $\mathbf{F}_v$, are expressed as:

$$\mathbf{F} = \begin{Bmatrix} \rho_1\mathbf{U} \\ \rho_2\mathbf{U} \\ \vdots \\ \rho_s\mathbf{U} \\ \rho u\mathbf{U} + \delta_{ij}p \\ \rho v\mathbf{U} + \delta_{ij}p \\ \rho w\mathbf{U} + \delta_{ij}p \\ (E+p)\mathbf{U} \\ E_{ve}\mathbf{U} \\ (E_e + p_e)\mathbf{U} \end{Bmatrix} \text{and } \mathbf{F}_{v,i} = \begin{Bmatrix} -J_{i,1} \\ -J_{i,2} \\ \vdots \\ -J_{i,s} \\ \tau_{i,x} \\ \tau_{i,y} \\ \tau_{i,y} \\ \tau_{ij}\mathbf{U}_j - \left(q_{tr} + \sum_s^{Allspecies} q_{ve,s} + q_e\right) - \sum(J_{i,s}h_s) \\ -\sum_s^{Allspecies} q_{ve,s} \\ \tau_{ij,e}\mathbf{U}_j - q_e - \left(J_{i,e}h_e\right) \end{Bmatrix} \tag{3}$$

where δ_{ij} denotes the Kronecker delta, $J_{i,s}$ is species diffusion flux in the i^{th} direction, and τ_{ij} are components of the viscous stress tensor. q_{tr}, q_{ve} and q_e are translational-rotational, vibrational-electronic, and electron heat flux, respectively. The viscous stresses are modelled using Stokes' hypothesis under the assumption of a Newtonian fluid, and the heat fluxes for each energy mode are formulated according to Fourier's law. Modified Fick's law is employed to model the species mass diffusion fluxes whilst enforcing the sum of the diffusion fluxes equating zero [16]. Wilke's semi-empirical mixing rule is utilised to model the mixture transport properties of viscosity, diffusion coefficients, and the thermal conductivity of each energy mode [17].

The thermochemical non-equilibrium source term, $\mathbf{S}_{NEQ}$, is described by

$$\mathbf{S}_{NEQ} = \begin{Bmatrix} \dot{\omega}_1 \\ \dot{\omega}_2 \\ \vdots \\ \dot{\omega}_s \\ 0 \\ 0 \\ 0 \\ 0 \\ S_{ve} \\ S_e \end{Bmatrix} \tag{4}$$

where $\dot{\omega}_s$ is the mass production rates of species s via chemical reactions, S_{ve} is the vibrational- electronic energy source term, and S_e is the electron energy source term. The vibrational-electronic energy source term, S_{ve}, can be described as:

$$S_{ve} = S_{ve-chem} + S_{ve-tr} + S_{vib-e} \tag{5}$$

where $S_{ve-chem}$ is the vibrational-electronic energy gained or removed by chemical reactions, S_{ve-tr} is the energy transferred between translational-rotational and vibrational-electronic modes, S_{vib-e} is the energy transfer between vibrational and electron energy modes. Radiative losses due to electronic transitions are not considered within this study. The electron energy source term, S_e, can be described as [18]:

$$S_e = S_{e-chem} + S_{e-tr} + S_{e-vib} \tag{6}$$

where S_{e-chem} is the electron energy gained or removed by chemical reactions, S_{e-tr} is the energy transferred between translational-rotational and electron energy modes, S_{e-vib} is the energy transfer between vibrational and electron modes. In this study, the work done on electrons by the electric field induced by the electron pressure gradient, $-p_e\nabla\cdot\mathbf{U}$, is not considered.

The source term related to MHD effects, $\mathbf{S}_{MHD}$, can be expressed as:

$$\mathbf{S}_{MHD} = \begin{Bmatrix} 0 \\ 0 \\ \vdots \\ 0 \\ (\mathbf{J}\times\mathbf{B})_x \\ (\mathbf{J}\times\mathbf{B})_y \\ (\mathbf{J}\times\mathbf{B})_z \\ \mathbf{E}\cdot\mathbf{J} \\ \beta\frac{\mathbf{J}\cdot\mathbf{J}}{\sigma} \\ (1-\beta)\frac{\mathbf{J}\cdot\mathbf{J}}{\sigma} \end{Bmatrix} \tag{7}$$

where we assume the entire energy of the Joule heating goes into the vibration-electronic and electron energies modes, and β describes the fraction of this heat going into each mode. The flow field equations are solved numerically using an in-house CFD code, HANSA, which discretises physical systems according to the finite volume method upon a block-structured Cartesian mesh.

To include MHD effects, we numerically solve Maxwell's equations with the generalised Ohm's law as:

$$\nabla^2 \phi = \nabla \cdot (\mathbf{U} \times \mathbf{B}) \tag{8}$$

and

$$\mathbf{j} = \sigma(\mathbf{E} + \mathbf{U} \times \mathbf{B}) \tag{9}$$

where the Hall and ion-slip effects are neglected with the low-magnetic Reynolds assumption. This implies that the ion-slip effect does not have a considerable influence on the electric current, and that the Hall effect does not have a negative influence on the MHD effects [19, 20]. The low magnetic Reynolds number assumption is applied because in the Newtonian limit, the typical magnetic Reynolds number is the order of 10^{-3} [21] in a weakly ionised gas which means the fraction of the ionized gas molecules is less than 10^{-4} [22].

2.2 Simulation geometry and boundary conditions

As part of a code verification and comparison study, an Argon flow system was chosen for numerical reproduction. This system simulated mirrors that of the experiments performed by Knapp et al. [23] with a magnetic probe immersed in an Argon plasma flow. The strength of the magnetic field issued by the probe was then varied, and the effect of this variation upon the plasma examined. The Knapp case experiments were originally conducted by IRS using their plasma wind tunnel PWK1, and showed a significant reduction in impinging heat loads when magnetic fields were applied. A schematic overview of the Knapp case's experimental setup, and the geometry of the magnetic probe are shown in Fig. 1.

Knapp's original experiments were performed with a variable magnetic probe to which small individual magnets were added to increase the magnetic field strength about the probe. This effect was simulated by manually aligning the magnetic field strength with the values used by Knapp. Simulations were performed with magnetic field strengths corresponding to zero, one and six magnets being present. The behaviour of these magnetic fields across the simulation domain has been computed using the *magpylib* python library [24]. The calculated magnetic field for 1-magnet and 6-magnet cases are shown in Figs. 2 and 3, respectively. The applied maximum magnetic field strength for 1-magnet and 6-magnet cases are 0.28 T and 0.36 T, respectively.

The measured plasma flow conditions for Knapp's experiments are listed in Table 1 [25], which were measured with intrusive techniques. These measured conditions are employed as inflow conditions in this study with the 3 species argon model (Ar, Ar^+, and e^-). The wall temperature at the probe's surface is assumed to be 300 K.

3 Results

3.1 In-house CFD code validation

3.1.1 Solver validation—I

The in-house non-equilibrium CFD solver, HANSA, is validated against several experimental and numerical results from the literature. In this section, we present the validation study performed against LeMANS, which is a finite volume solver developed at the University of Michigan [26]. This problem involves hypersonic flow over a 2D cylinder with a diameter of 0.3048 m at two different Mach numbers, 10

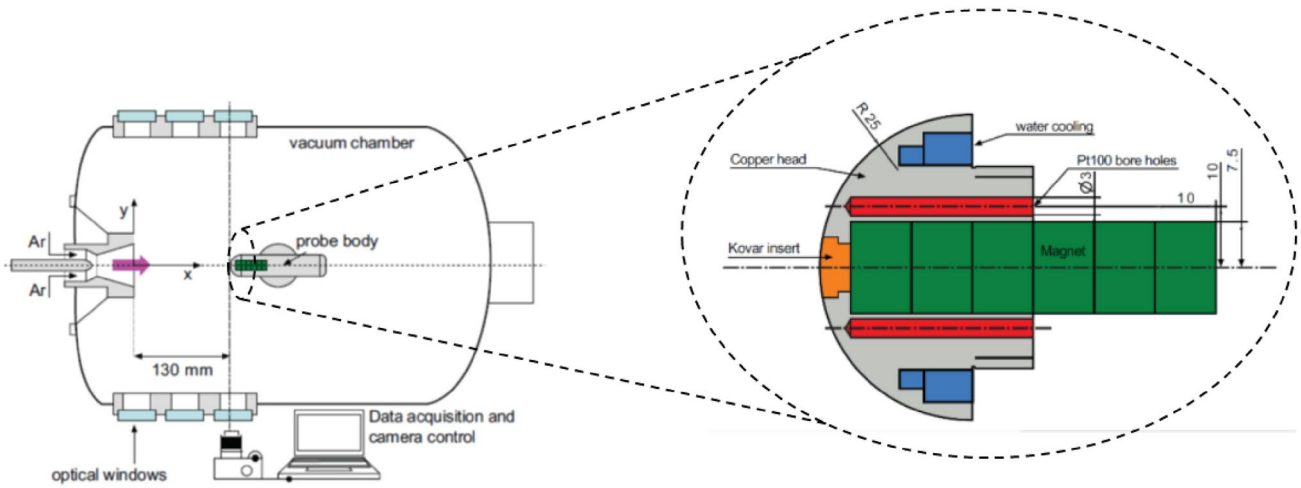

Fig. 1 Schematic overview of the original Knapp experimental setup together with schematic of the utilised magnetic probe (magnified on the right image). Images courtesy of IRS Stuttgart

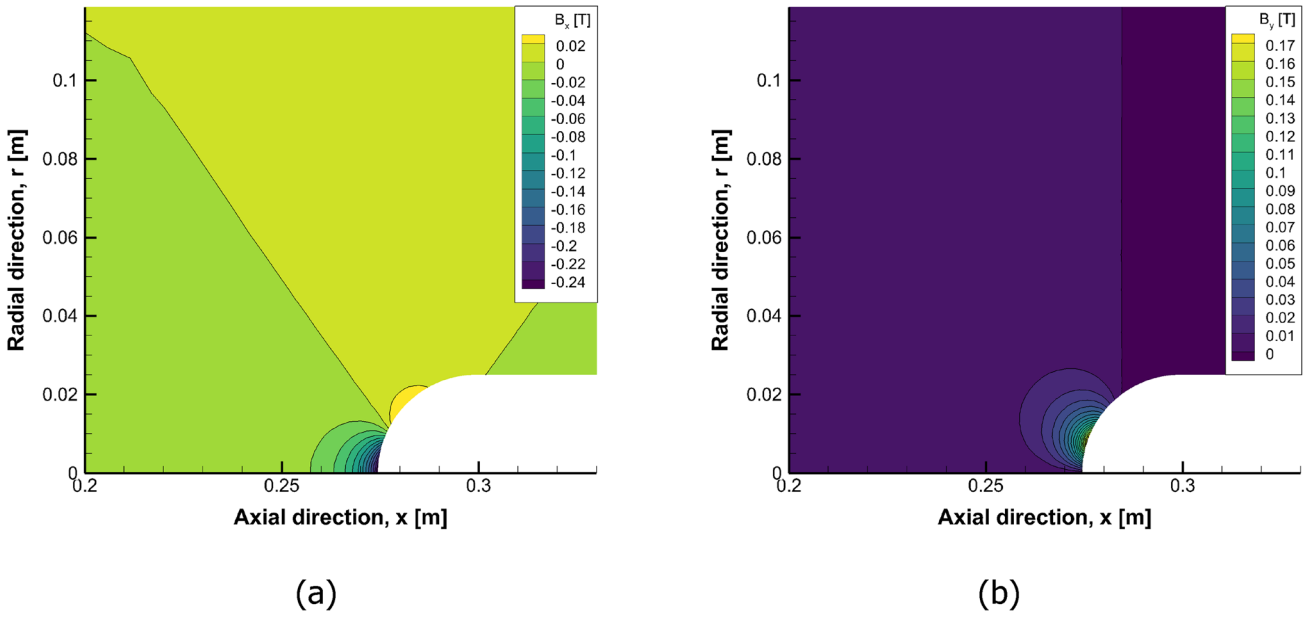

Fig. 2 Configuration of the applied magnetic field for the 1 magnet case; **a** Azimuthal direction magnetic field. **b** Radial direction magnetic field

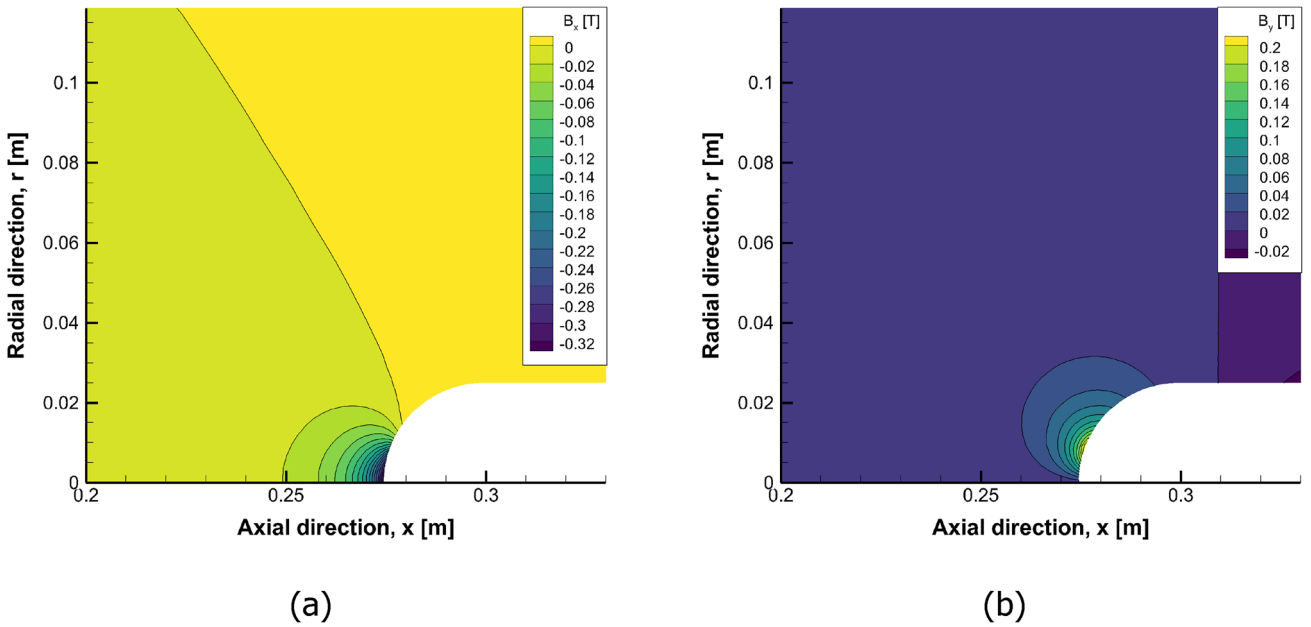

Fig. 3 Configuration of the applied magnetic field for the 6 magnet case; **a** Azimuthal direction magnetic field**. b** Radial direction magnetic field

and 25. The freestream conditions are taken from Lofthouse et al. [27], and nitrogen is considered as the gas species. The Knudsen number, based on the cylinder diameter, is 0.002, placing it in the slip regime where the continuum models are still applicable (at least for validation purposes) and the freestream temperature is set to 200 K for both cases. The wall temperature is fixed at 500 K and 1500 K for the Mach 10 and 20 cases, respectively. We employ the Modified Steger-Warming (MSW) vector splitting approach to compute inviscid fluxes, except at the shock where the original S-W method is used, whereas viscous fluxes are computed using properties at the cell centers. A point implicit algorithm is applied for time integration.

The density, translational, and vibrational temperature flow contours predicted by the HANSA solver are compared with those from the LeMANS solver, as shown in Fig. 4. It

Table 1 Measured plasma flow conditions for Knapp's experiments [25]

Total pressure	240 ± 5 Pa
Heat flux	1263 ± 108 kW/m^2
Mass specific enthalpy	25.7 ± 4.6 MJ/kg
Electron temperature	17377 ± 2604 K
Electron density	$7.38 \pm 0.1 \times 10^{19}$m^{-3}
Velocity	3100 m/s
Heavy particle temperature	8700 K
Ionisation degree	0.3

is evident that the variations in flow properties predicted by HANSA closely align with the results obtained from LeMANS [27]. The translational and vibrational temperature variations along the stagnation streamline are also compared with LeMANS at Mach numbers 10 and 25, as shown in Fig. 5. The variation of properties including the shock standoff distance and peak temperature are in very good agreement with LeMANS, presented in Lofthouse et al. [27].

3.1.2 Solver validation—II

In this section, we compare the results obtained from HANSA with an experimental study conducted by Karl et al. [28], which is commonly used as a test case for verifying non-equilibrium solutions [29, 30]. This study involves a high enthalpy flow over a cylinder with a radius of 45 mm and a span of 380 mm in the High Enthalpy Shock Tunnel Göttingen (HEG). Due to the large span length in comparison to the radius, this problem is assumed to be two-dimensional in HANSA. The freestream conditions for this case are presented in Table 2.

In this case, the vibrational-translational (VT) energy exchange is modelled via the Landau-Teller formula [31] and the vibrational relaxation time is calculated through a Millikan-White correlation [32] with Park's correction [33, 34]. The chemical reactions are modelled using a finite rate chemistry model and the rate coefficients are evaluated using Park's two-temperature model. The surface pressure variation observed from HANSA is compared with the experimental results, as shown in Fig. 6. It has been found that the results obtained from HANSA are in good agreement with the experimental data. There is a minor discrepancy between the results at the stagnation point, with a maximum difference of 2.5%. The variation of mass fraction of all species along the stagnation streamline is also shown in Fig. 6 (right). After the shock ($x \sim 0.0096$ m), the nitrogen molecules dissociate, resulting in a decrease in N_2 fraction and an increase in nitrogen atoms. The recombination of nitrogen atoms is more pronounced close to the surface, as indicated by an increase in N_2 and a decrease in N fractions. This trend is consistent with Adhikari's findings for the same case [35]; however, the results are not directly compared here due to differences in reaction models.

3.2 Schiaparelli capsule Martian atmospheric entry

Investigations of magnetic re-entry systems require the ability to reconstruct the behaviour of real capsules in atmospheric entry conditions. In this study, we have selected the

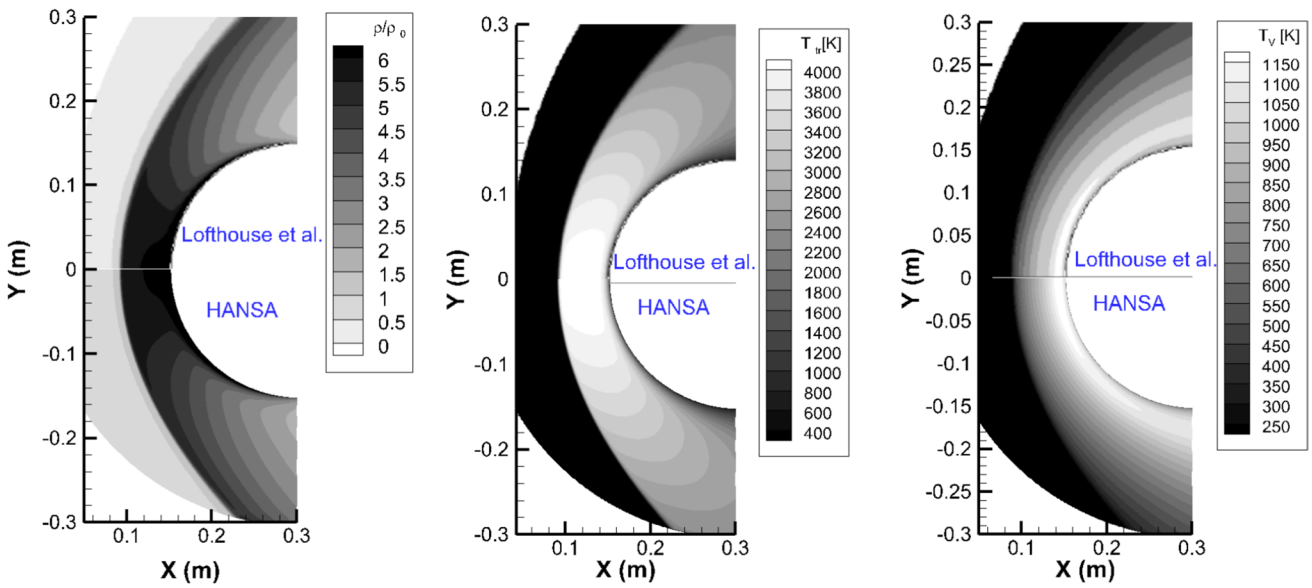

Fig. 4 Flow contour of density ratio (normalised with freestream density), translation and vibrational temperatures obtained from HANSA (bottom) compared with LeMANS, presented in Lofthouse et al. [27] (top)

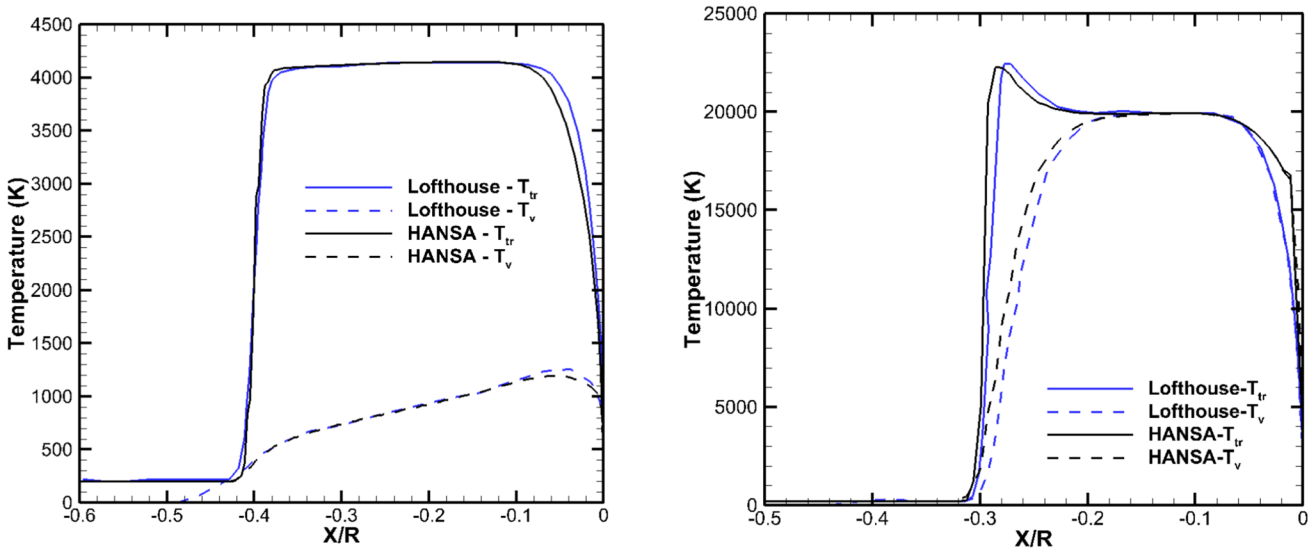

Fig. 5 Comparison of translational and vibrational temperature variation along the stagnation streamline obtained from HANSA with LeMANS from Lofthouse et al. [27]. The x-axis represents the negative distance from the stagnation point, normalised with the cylinder radius

Table 2 Freestream conditions for HEG cylinder from Karl et al. [28]

Velocity	4776 m/s
Mach Number	8.78
Density	0.00326 kg/m^3
Molar fractions	
Y_{N_2}	0.735
Y_{O_2}	0.134
Y_{NO}	0.0509
Y_N	0.0
Y_O	0.07955

ExoMars Schiaparelli capsule to validate the implemented thermo-chemical non-equilibrium models in HANSA due to the availability of real-world data following its entry into Martian atmosphere [36, 37]. Figure 7 shows the geometry of the Schiaparelli capsule which is a typical blunt body re-entry vehicle. The forebody shape of the Schiaparelli capsule is composed of a spherical nose with a 0.6 m radius, a cone, and a circular shoulder. The inflow conditions of the Schiaparelli capsule are listed in Table 3, which corresponds to the conditions at an altitude of 56 km. In this study, the freestream flow for the Martian atmosphere is assumed to

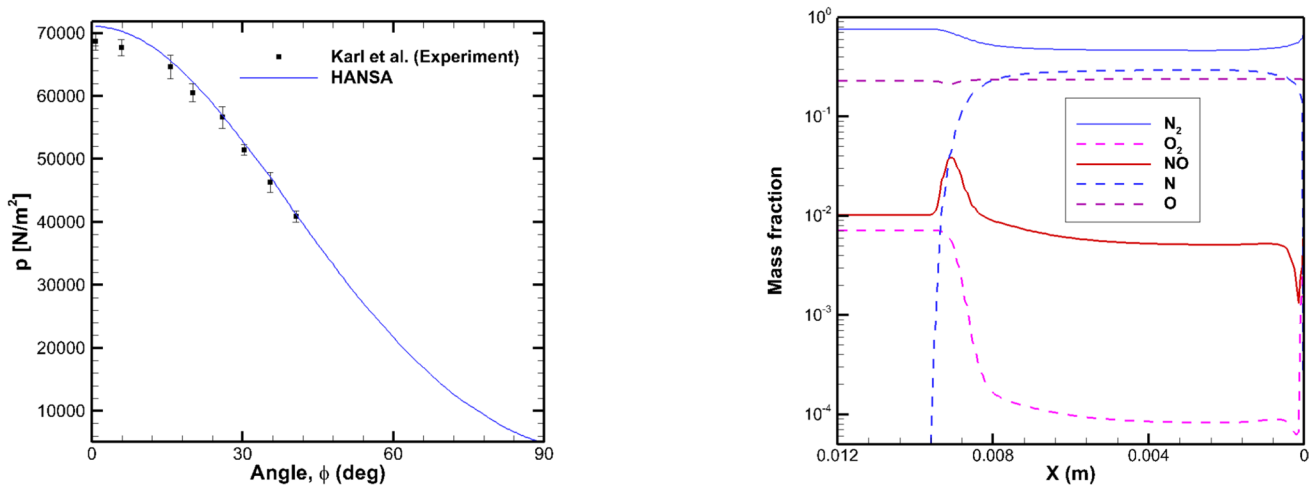

Fig. 6 Comparison of surface pressure variation along the cylinder obtained from HANSA with experimental results from Karl et al. [28] (left). The mass fraction variation along the stagnation streamline (right)

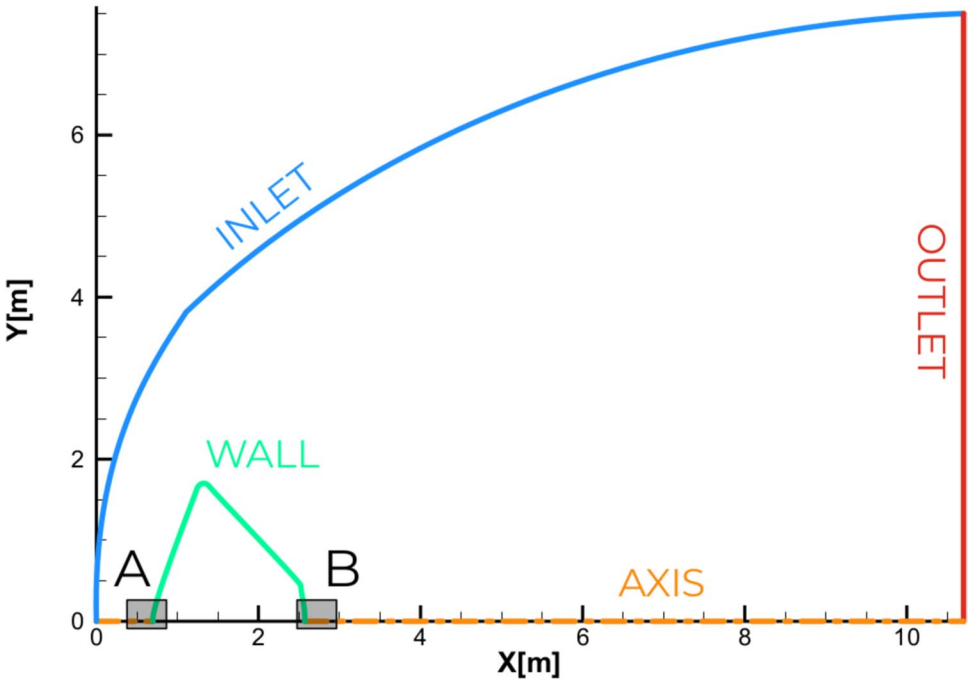

Fig. 7 Simulation domain of the Schiaparelli capsule

Table 3 Inflow conditions of the simulation which correspond to the 56 km altitude entry condition of the Schiaparelli capsule

Inflow velocity, V_∞	4516 m/s
Freestream temperature, T_∞	174 K
Freestream density, ρ_∞	5.82×10^{-4} kg/m^{-3}
Freestream mole fraction	$X_{CO_2} = 0.96; X_{N_2} = 0.04$
Wall temperature, T_{wall}	1500 K

be steady and laminar with the composition of 96% CO_2 and 4% N_2. The vehicle walls are assumed non-catalytic and isothermal, with a wall temperature of 1500 K.

Figure 8 shows the temperature contour alongside the Mach number contour. A disk shock is formed due to the interaction of expansion waves with the reversed flow, as illustrated by the streamlines and Mach contour in Fig. 8b). A similar phenomenon has previously been observed by

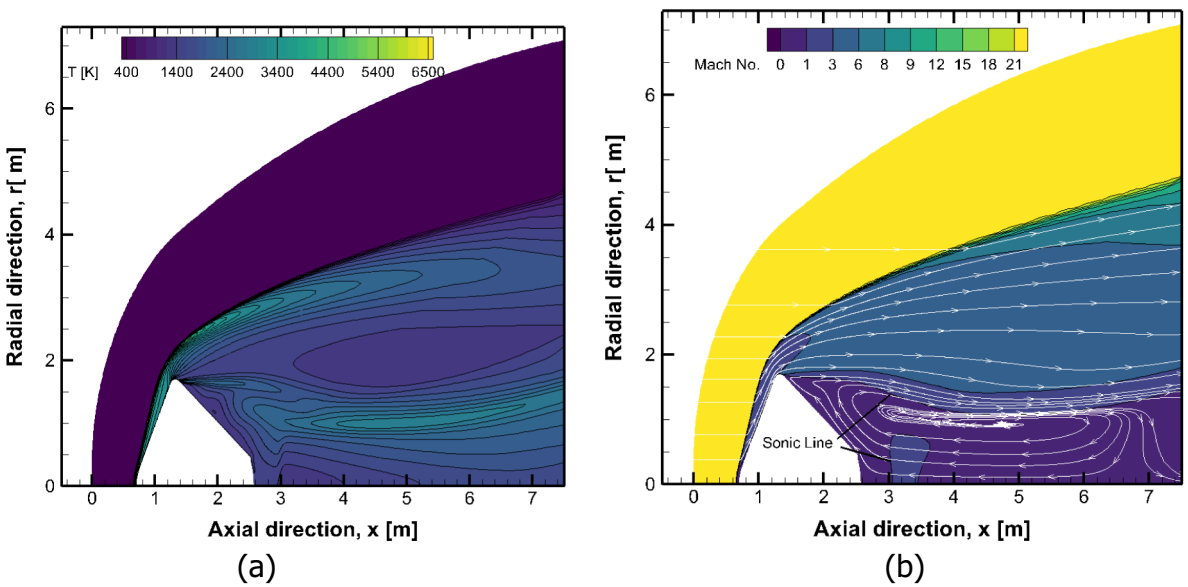

Fig. 8 Temperature contour of the Schiaparelli capsule at 56 km entry condition; **a** Translational-rotational temperature **b** Mach number

Wright et al. [38] for the Phoenix aeroshell during Mars entry. The normalised electron number density contour is also shown in Fig. 9, with the number density normalised to the critical number density for the Mars Pathfinder ($n_{crictical} = 8.75 \times 10^{17} m^{-3}$) [10]. The majority of electrons are concentrated in the bow shock and post-shock regions, where the number density exceeds the critical number density. In contrast, the electron number density in the wake region is below the critical number density for a communication blackout.

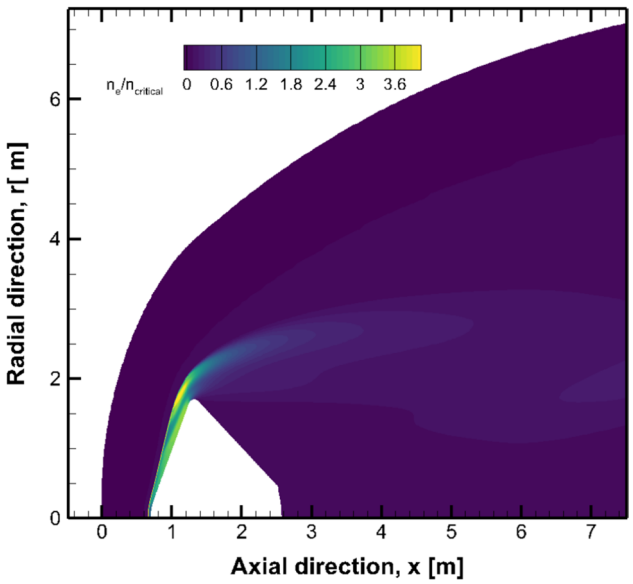

Fig. 9 Normalised electron number density of the Schiaparelli capsule at 56 km entry condition

3.3 MHD effects

In this section, we discuss the effects of MHD on flow and surface properties by placing magnets. Figures 10 and 11 show, respectively, heavy particle temperature and electron temperature contours near the Knapp's probe with and without the magnetic field. As can be seen, the location of the shock is shifted due to the MHD effects, specifically the Lorentz force, which is induced by the applied magnetic field. The shock-stand-off distance for the 6-magnet case is found to be higher than that for the 1-magnet case. Therefore, a stronger magnetic field leads to a larger enhancement of the shock standoff distance. This results in reduced gas and electron temperature near the vehicle surface.

To find the effects of MHD on surface heat flux, Table 4 compares the peak heat flux with and without a magnetic field, alongside experimental data from Knapp's study [25]. As can be observed, the model accurately predicts the heat flux measured in the experiment when no magnetic field is applied. However, when a magnetic field is introduced, the model predicts a reduction in peak heat flux of 10% and 16% for the 1-magnet and 6-magnet configurations, respectively. This reduction occurs because the electromagnetic field pushes the plasma layer away from the probe, thereby increasing the shock stand-off distance. Although this increased stand-off distance does not directly affect the thermo-chemical non-equilibrium process, it increases

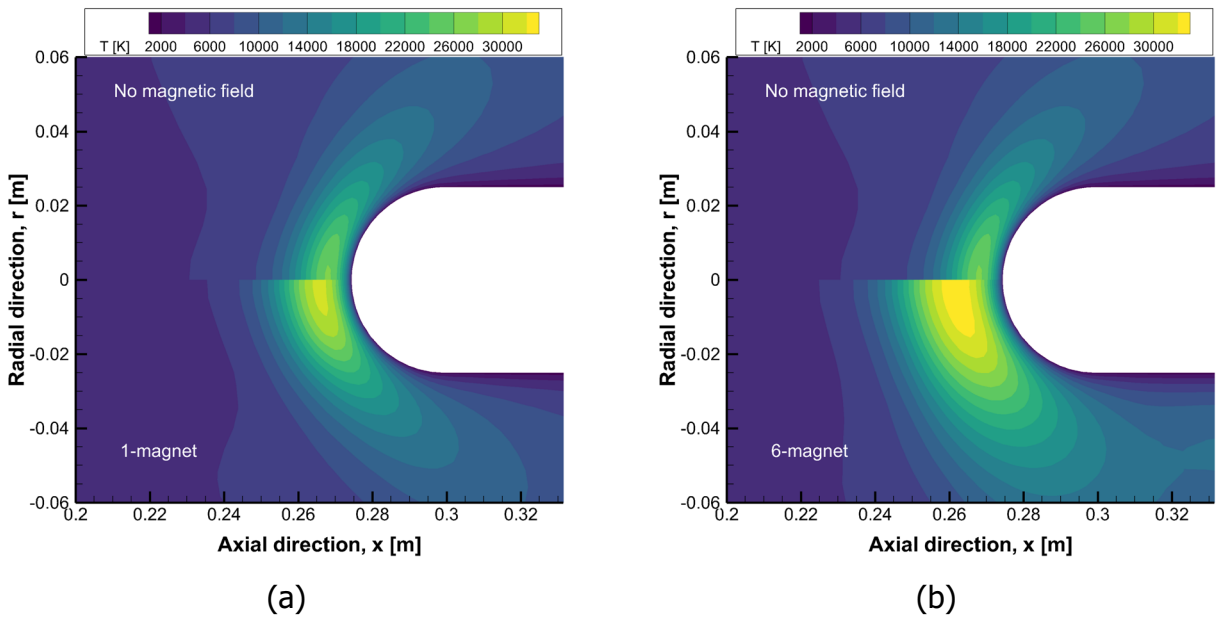

Fig. 10 Heavy particle temperature fields, T, proximate to the probe nose for 1 and 6 magnets compared with the 0 magnet case. **a** 1-magnet case. **b** 6-magnet case

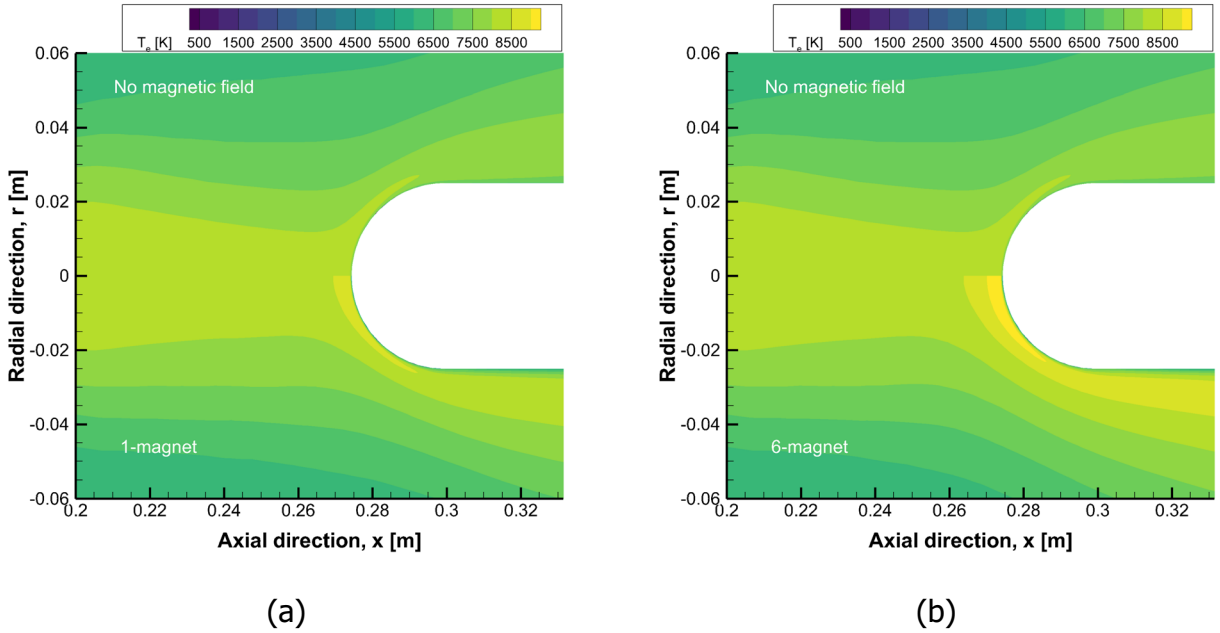

Fig. 11 Electron temperature fields, T_e, proximate to the probe nose for 1 and 6 magnets compared with the 0 magnet case. **a** 1-magnet case. **b** 6-magnet case

energy dissipation, leading to reduced heat flux. Additionally, due to the magnetic field and plasma around the vehicle, a temperature gradient could develop within the probe as a result of the Ettingshausen effect, where the magnetic field interacts with electrical currents in the plasma to generate transverse temperature differences. This effect, however, is not considered in this study, as the material perspective is beyond the scope of this paper. Since experimental data for these specific magnet configurations are unavailable, simulations with a magnetic field are not directly compared to experimental values in these cases.

4 Conclusion

In this study, we have presented a series of simulations conducted using the University of Southampton's HANSA Computational Fluid Dynamics (CFD) toolkit within the framework of the Magnetic Enhanced Entry Systems for Space Transportation (MEESST) project. The MEESST project aims to pioneer innovative magnetic plasma control methods for spacecraft re-entry. A concise overview of the methodology employed by HANSA is provided to offer context and promote the reproducibility of the presented results. The simulations are contextualized within the broader scope of the MEESST project, with concurrent experimental endeavors by MEESST collaborators being outlined. The outcomes encompass simulations illustrating heat flux manipulation using MHD effects, along with comprehensive capsule simulations.

The three showcased simulation campaigns herein underscore HANSA's proficiency in contributing to the advancement of magnetic plasma control systems and its capability simulating thermo-chemical non-equilibrium flows. A code-to-code comparison of HANSA against LeMANS showcases the accuracy of the thermo-chemical non-equilibrium models implemented in HANSA. The results from the Knapp case illustrate the effective manipulation of Argon plasma under magnetic influence. Likewise, the Schiaparelli simulations underscore HANSA's capacity to simulate entire capsules, encompassing intricate thermo-chemical interactions, within a Martian atmosphere. These endeavors underscore the ability of MEESST collaborators to consistently simulate systems pertinent to magnetic plasma manipulation aboard re-entry spacecraft.

This capability will be further leveraged in the remaining phases of the MEESST project to compile a comprehensive

Table 4 Comparison of peak stagnation heat flux against the experimental results from Knapp's study [25]

	No magnetic field	1-magnet case	6-magnet case
Experiment [25]	$1235.38 \pm 200 \mathrm{kW/m^2}$	–	–
Simulation	1407.7 kW/m^2	1274.9 kW/m^2	1182.1 kW/m^2

dataset showcasing the effects of magnetic plasma manipulation. This dataset will facilitate comparisons with previous studies utilizing Argon plasma, providing insights into the influence of plasma composition on magnetic responsiveness. Such research avenues hold promise for future investigations utilizing Martian atmosphere plasma, potentially offering valuable insights for missions within the Artemis program and beyond.

Acknowledgements The authors would like to thank the other members of the MEESST consortium for the key work that they've undertaken. Without their contributions, the work within this paper would not have been possible. This work was made possible by the Future and Emerging Technologies (FET) programme within the European Commission's Horizon 2020 scheme [grant no. 899298]. The authors would also like to acknowledge use of the IRIDIS high performance compute cluster at the University of Southampton and offer thanks to the IRIDIS team.

Author contributions T.G: developing models, running simulations, manuscript writing, preparing figures and revisions. A.C: developing models, running simulations, manuscript writing, preparing figures and revisions. M.K: guidance, developing models, funding acquisition, manuscript writing and revisions. All authors reviewed the manuscript.

Funding European Commission's Horizon 2020 scheme, 899298.

Data availability No datasets were generated or analysed during the current study.

Declarations

Conflict of interest The authors declare no competing interests.

References

1. Erb, A.J., West, T.K., Johnston, C.O.: Investigation of Galileo probe entry heating with coupled radiation and ablation. J. Spacecr. Rocket. **57**(4), 692–706 (2020). https://doi.org/10.2514/1.A34751
2. Edquist, K., Dyakonov, A., Wright, M., Tang, C.: Aerothermodynamic design of the Mars science laboratory heatshield. 41 st AIAA Thermophys Conf. (2009). https://doi.org/10.2514/6.2009-4075
3. Stalder J. R., Nielsen, H. V.: Heat transfer from a hemisphere-cylinder equipped with flow-separation spikes. NACA-TN-3287 (1954).
4. Chinnappan, A.K., Malaikannan, G., Kumar, R.: Insights into flow and heat transfer aspects of hypersonic rarefied flow over a blunt body with aerospike using direct simulation Monte-Carlo approach. Aerosp. Sci. Technol. **66**, 119–128 (2017). https://doi.org/10.1016/j.ast.2017.02.024
5. Mohammed Ibrahim, S., Vivek, P., Reddy, K.P.J.: Experimental investigation on transpiration cooling effectiveness for spacecraft entering Martian atmosphere. AIAA J. **54**(9), 2922–2926 (2016). https://doi.org/10.2514/1.J054757
6. Gülhan, A., Braun, S.: An experimental study on the efficiency of transpiration cooling in laminar and turbulent hypersonic flows. Exp. Fluids **50**, 509–525 (2011). https://doi.org/10.1007/s00348-010-0945-6
7. Ifti, H.S., Hermann, T., Ewenz Rocher, M., Doherty, L., Hambidge, C., McGilvray, M., Vandeperre, L.: Laminar transpiration cooling experiments in hypersonic flow. Exp. Fluids **63**(6), 102 (2022). https://doi.org/10.1007/s00348-022-03446-1
8. Romeo, D. J., Sterrett, J. R.: Exploratory investigation of the effect of a forward-facing jet on the bow shock of a blunt body in a Mach number 6 free stream. *NASA Technical Note, D-1605* (1963).
9. Gerdroodbary, M.B., Fayazbakhsh, M.A.: Numerical study on heat reduction of various counterflowing jets over highly blunt cone in hypersonic flow. Int J Hypersonics **2**, 1–13 (2012). https://doi.org/10.1260/1759-3107.2.1.1
10. Kim, M. K.: Electromagnetic manipulation of plasma layer for re-entry blackout mitigation. *PhD Thesis, University of Michigan* (2009).
11. Hartunian, R., Stewart, G., Curtiss, T., Fergason, S., Seibold, R., Shome, P.: Implications and mitigation of radio frequency blackout during reentry of reusable launch vehicles. AIAA Atmos Flight Mech Conf Exhibit. (2007). https://doi.org/10.2514/6.2007-6633
12. Rybak, J.P., Churchill, R.J.: Progress in reentry communications. IEEE Trans. Aerosp. Electron. Syst. **5**, 879–894 (1971). https://doi.org/10.1109/TAES.1971.310328
13. Lani, A., Sharma, V., Giangaspero, V.F., Poedts, S., Viladegut, A., Chazot, O., Bögel, E.: A Magnetohydrodynamic enhanced entry system for space transportation: MEESST. J Space Safety Eng **10**(1), 27–34 (2023). https://doi.org/10.1016/j.jsse.2022.11.004
14. Desiati, P., & D'Onghia, E.: CREW HaT: A Magnetic Shielding System for Space Habitats. *arXiv preprint* arXiv:2209.13624 *(2022). Accessed 07 November 2024.*
15. Ferrone, K., Willis, C., Guan, F., Ma, J., Peterson, L., Kry, S.: A review of magnetic shielding technology for space radiation. Radiation **3**(1), 46–57 (2023). https://doi.org/10.3390/radiation3010005
16. Sutton, K., Gnoffo, P.: Multi-component diffusion with application to computational aerothermodynamics. *In 7th AIAA/ASME Joint Thermophysics and Heat Transfer Conference.* (1998). https://doi.org/10.2514/6.1998-2575
17. Wilke, C.R.: A viscosity equation for gas mixtures. J. Chem. Phys. **18**(4), 517–519 (1950). https://doi.org/10.1063/1.1747673
18. Kim, M., Boyd, I.D.: Effectiveness of a magnetohydrodynamics system for Mars entry. J. Spacecr. Rocket. **49**(6), 1141–1149 (2012). https://doi.org/10.2514/1.A32256
19. Fujino, T., Sugita, H., Mizuno, M., Funaki, I., Ishikawa, M.: Influences of electrical conductivity of wall on magnetohydrodynamic control of aerodynamic heating. J. Spacecr. Rocket. **43**(1), 63–70 (2006). https://doi.org/10.2514/1.13770
20. Morris, D., Gilchrist, B., Gallimore, A., Jensen, K.: Developing field emitter array cathode systems for electrodynamic tether propulsion. *In 36th AIAA/ASME/SAE/ASEE Joint Propulsion Conference and Exhibit (p. 3867)* (2000). https://doi.org/10.2514/6.2000-3867

21. Shang, J., Menart, J., Kimmel, R., Hayes, J.: Hypersonic inlet with plasma induced compression. 44th *AIAA Aerospace Sciences Meeting and Exhibit* (2006). https://doi.org/10.2514/6.2006-764
22. Parent, B., Shneider, M.N., Macheret, S.O.: Generalized ohm's law and potential equation in computational weakly-ionized plasmadynamics. J. Comput. Phys. **230**(4), 1439–1453 (2011). https://doi.org/10.1016/j.jcp.2010.11.012
23. Knapp, A., Fulge, H., Herdrich, G., Ono, N., Wernitz, R., Auweter-Kurtz, M., Fasoulas, S.: Investigation of MHD impact on Argon plasma flows by variation of magnetic flux density. Open Plasma Phys J. (2012). https://doi.org/10.2174/1876534301205010011
24. Ortner, M., Bandeira, L.G.C.: Magpylib: a free Python package for magnetic field computation. SoftwareX **11**, 100466 (2020). https://doi.org/10.1016/j.softx.2020.100466
25. Knapp, A. J.: Experimentelle Untersuchung von magnetohydrodynamischen Einflüssen auf Plasmaströmungen, *PhD thesis, Institut für Raumfahrtsysteme, Universität Stuttgart* (2012).
26. Scalabrin, L. C.: Numerical simulation of weakly ionized hypersonic flow over reentry capsules, *PhD thesis, University of Michigan* (2007).
27. Lofthouse, A. J.: Nonequilibrium Hypersonic Aerothermodynamics Using the Direct Simulation Monte Carlo and Navier-Stokes Models, *PhD thesis, University of Michigan* (2008).
28. Karl, S., Martinez Schramm, J., & Hannemann, K.: High enthalpy cylinder flow in HEG: A basis for CFD validation. *In 33rd AIAA Fluid Dynamics Conference and Exhibit*. p. 4252 (2003). https://doi.org/10.2514/6.2003-4252
29. Gimelshein, S.F., Wysong, I.J.: Nonequilibrium air flow predictions with a high-fidelity direct simulation Monte Carlo approach. Phys Rev Fluids **4**(3), 033405 (2019). https://doi.org/10.1103/PhysRevFluids.4.033405
30. Knight, D., Longo, J., Drikakis, D., Gaitonde, D., Lani, A., Nompelis, I., Walpot, L.: Assessment of CFD capability for prediction of hypersonic shock interactions. Prog. Aerosp. Sci. **48**, 8–26 (2012). https://doi.org/10.1016/j.paerosci.2011.10.001
31. Vincenti, W.G., Kruger, C.H.: Introduction to physical gas dynamics. Krieger Publishing Company, New York (1982)
32. Millikan, R.C., White, D.R.: Systematics of vibrational relaxation. J. Chem. Phys. **39**(12), 3209–3213 (1963). https://doi.org/10.1063/1.1734182
33. Park, C.: Review of chemical-kinetic problems of future NASA missions, I : Earth entries. J. Thermophys. Heat Transfer **7**(3), 385–398 (1993). https://doi.org/10.2514/3.431
34. Park, C.: Nonequilibrium hypersonic aerothermodynamics. John Wiley & Sons, New York (1990)
35. Adhikari, N.: Investigation of Aerothermodynamic and Chemical Kinetic Models for High-Speed Nonequilibrium Flows. *Doctoral dissertation, Purdue University* (2021).
36. Ball, A.J., Blancquaert, T., Bayle, O., Lorenzoni, L.V., Haldemann, A.F.: Schiaparelli EDM team: the ExoMars schiaparelli entry, descent and landing demonstrator module (EDM) system design. Space Sci Rev **218**(5), 44 (2022). https://doi.org/10.1007/s11214-022-00898-z
37. Bonetti, D., De Zaiacomo, G., Blanco, G., Fuentes, I.P., Portigliotti, S., Bayle, O., Lorenzoni, L.: ExoMars 2016: Schiaparelli coasting, entry and descent post flight mission analysis. Acta Astronaut. **149**, 93–105 (2018). https://doi.org/10.1016/j.actaastro.2018.05.029
38. Wright, M., Edquist, K., Tang, C., Hollis, B., Krasa, P., Campbell, C.: A review of aerothermal modeling for Mars entry missions. *In 48th AIAA Aerospace Sciences Meeting Including the New Horizons Forum and Aerospace Exposition (p. 443)* (2010). https://doi.org/10.2514/6.2010-443